H_6 and mBDCA-5p-H_6 in oxygen-saturated DMF solution. An increase in the limiting current as well as decreasing slope of the Koutecký-Levich (K-L) analysis of diffusion-limited currents (Fig. 3B, inset) is consistent with a greater number of electrons transferred during reduction of oxygen in the presence of mBDCA-5t-H_6 than the one-electron reduction process without mBDCA-5t-H_6 (20). A large excess of cryptand is needed in order to drive the electrochemical process completely to peroxide encapsulation during rotating-disk electrode experiments. K-L analysis of diffusion-limiting currents as a function of the inverse square root of rotation speed, collected in 0.1 M [TBA][ClO$_4$] DMF solution saturated with 1% O_2 in argon with 4.8 mM mBDCA-5t-H_6 (Fig. 3C), indicates that the number of transferred electrons increases toward an overall two-electron process, which is expected if every oxygen molecule was reduced and encapsulated by the cryptand.

Figure 3D shows a simulation of the cyclic voltammogram using the reaction sequence illustrated in Fig. 4. The reaction sequence used to model the electrochemistry concurs with the established chemical reactivity of O_2 and cryptand described by Fig. 1. Parameters obtained from the simulation are collected in table S5, a and b. Our model suggests that rapid encapsulation of O_2^- by free cryptand drives further one-electron reduction, either directly by the working electrode or through a disproportionation reaction with another equiv of O_2^-, resulting in the formation of $[(O_2) \subset m\text{BDCA-5t-}H_6]^{2-}$. The assumption that the diffusion coefficient of O_2 is much greater than that of the cryptand species (table S5b) in DMF containing 0.1 M [TBA][ClO$_4$] reproduces the sharp feature observed before the wave attributed to one-electron reduction of O_2. An appropriate fit for the anodic sweep could only be accomplished by modeling the oxidation of $[(O_2) \subset m\text{BDCA-5t-}H_6]^{2-}$ as a series of two, one-electron oxidations.

The reversible one-electron reduction of oxygen in DMF is altered by addition of both strong and weak acids (21). In the case of mBDCA-5t-H_6, the cryptand could serve as a source of protons. However, figs. S27 and S28 illustrate that the reduction of oxygen in the presence of strong and weak acids, respectively, differs from oxygen reduction in the presence of mBDCA-5t-H_6 at equal concentration. These data suggest that the cryptand does not serve as a Brønsted acid in the overall oxygen reduction process.

The electrochemistry of mBDCA-5t-H_6 and mBDCA-5p-H_6 in the presence of oxygen is consistent with reduction of oxygen by one electron to superoxide followed by incorporation into the cryptand cavity, in turn driving disproportionation to give the cryptand-encapsulated peroxide adduct. Oxidation of peroxide dianion within the cavity restores oxygen and the free cryptand ligand. The proposed electrochemical mechanism in Fig. 4 maps on to the observed chemical reactivity of Fig. 1; the combined chemical and electrochemical studies demonstrate encapsulation-driven

chemically reversible two-electron reduction of O_2 to peroxide dianion.

We have synthesized a molecular peroxide dianion adduct by the use of the cavity of hexacarboxamide cryptands as a molecular recognition site. Reduction of oxygen in situ and stabilization of peroxide dianion is facilitated by hydrogen bonding within the cavity of the cryptand, and this process mimics the structural characteristics of biological systems that use peroxide as an oxidant. The use of molecular recognition of an in situ–generated reactive oxygen species has the potential to be incorporated into several technologies, including Li-air batteries, because it is chemically reversible, prevents over-reduction to lithium oxide, and imparts substantial solubility in aprotic media (22). In addition, because the present peroxide adducts can be obtained in high yield in a one-pot reaction and are stable in solution, they could be used as a soluble source of peroxide dianion for a variety of reactions.

References and Notes

1. B. Meunier, Ed., *Metal-Oxo and Metal-Peroxo Species in Catalytic Oxidations* (Springer, Berlin, 2000).
2. B. Meunier, Ed., *Biomimetic Oxidations Catalyzed by Transition Metal Complexes* (Imperial College Press, London, 2000).
3. B. Meunier, S. P. de Visser, S. Shaik, *Chem. Rev.* **104**, 3947 (2004).
4. A. Butler, M. J. Clague, G. E. Meister, *Chem. Rev.* **94**, 625 (1994).
5. M. V. George, K. S. Balachandran, *Chem. Rev.* **75**, 491 (1975).
6. T. Kato et al., *Chem. Lett.* **39**, 136 (2010).
7. M. Grehl, R. Fröhlich, S. Thiele, *Acta Crystallogr. C* **51**, 1038 (1995).
8. S. O. Kang, J. M. Llinares, D. Powell, D. VanderVelde, K. Bowman-James, *J. Am. Chem. Soc.* **125**, 10152 (2003).
9. S. O. Kang, V. W. Day, K. Bowman-James, *J. Org. Chem.* **75**, 277 (2010).
10. G. E. Alliger, P. Müller, C. C. Cummins, D. G. Nocera, *Inorg. Chem.* **49**, 3697 (2010).
11. G. E. Alliger, P. Müller, L. H. Do, C. C. Cummins, D. G. Nocera, *Inorg. Chem.* **50**, 4107 (2011).
12. J. L. Sessler, P. A. Gale, W.-S. Cho, *Anion Receptor Chemistry* (Royal Society of Chemistry, London, ed. 1, 2006).
13. M. Garcia-Viloca, A. González-Lafont, J. M. Lluch, *J. Am. Chem. Soc.* **119**, 1081 (1997).
14. A. K. Boal, J. A. Cotruvo Jr., J. Stubbe, A. C. Rosenzweig, *Science* **329**, 1526 (2010).
15. R. D. Jones, D. A. Summerville, F. Basolo, *Chem. Rev.* **79**, 139 (1979).
16. G. R. Desiraju, T. Steiner, in *The Weak Hydrogen Bond in Structural Chemistry and Biology* (Oxford Univ. Press, Oxford, 1999), p. 13.
17. The residual electron density of refinements without assignment of the electron density of N–H hydrogen atoms surrounding the peroxide moiety suggests that the protons reside at the carboxamide nitrogens of the cryptand, even though the exact position cannot be obtained from x-ray data. Thus, hydroperoxide anion HO$_2^-$ is unlikely to be the species trapped, and the best model obtained was of peroxide dianion (figs. S29 to S32).
18. N. Bartlett, F. O. Sladky, *Chem. Commun.* **1968**, 1046 (1968).
19. D. L. Maricle, W. G. Hodgson, *Anal. Chem.* **37**, 1562 (1965).
20. A. J. Bard, L. R. Faulkner, in *Electrochemical Methods: Fundamentals and Applications* (Wiley, New York, ed. 2, 2000), p. 341.
21. D. T. Sawyer, G. Chiericato Jr., C. T. Angelis, E. J. Nanni Jr., T. Tsuchiya, *Anal. Chem.* **54**, 1720 (1982).
22. G. Girishkumar, B. McCloskey, A. C. Luntz, S. Swanson, W. Wilcke, *J. Phys. Chem. Lett.* **1**, 2193 (2010).

A Long-Lived Lunar Core Dynamo

Erin K. Shea,[1]* Benjamin P. Weiss,[1] William S. Cassata,[2] David L. Shuster,[2,3] Sonia M. Tikoo,[1] Jérôme Gattacceca,[4] Timothy L. Grove,[1] Michael D. Fuller[5]

Paleomagnetic measurements indicate that a core dynamo probably existed on the Moon 4.2 billion years ago. However, the subsequent history of the lunar core dynamo is unknown. Here we report paleomagnetic, petrologic, and $^{40}\text{Ar}/^{39}\text{Ar}$ thermochronometry measurements on the 3.7-billion-year-old mare basalt sample 10020. This sample contains a high-coercivity magnetization acquired in a stable field of at least ~12 microteslas. These data extend the known lifetime of the lunar dynamo by 500 million years. Such a long-lived lunar dynamo probably required a power source other than thermochemical convection from secular cooling of the lunar interior. The inferred strong intensity of the lunar paleofield presents a challenge to current dynamo theory.

The discovery of remanent magnetization in samples taken by the Apollo lunar missions and by spacecraft observations of the lunar crust has long suggested that the Moon formed a metallic core and a dynamo-generated

magnetic field (1). However, the association of magnetization with the antipodes of impact basins and laboratory studies of transient plasma-generated magnetic fields suggest that meteoroid impacts could also be a source of lunar magnetization (2, 3).

Because impact fields from the largest basin-forming events are expected to last less than 1 day (2), they should only be recorded by shocked or quickly cooled rocks. Therefore, to identify records of a core dynamo field, it is important to study slowly cooled samples with high magnetic recording fidelity that show no petrographic evidence of shock. Unfortunately, few lunar rocks have all of these properties (1). An exception is lunar troctolite sample 76535, which was observed to have a stable natural remanent magnetization (NRM) formed in a field of ~1 to 50 µT that is stable up to coercivities >200 mT (4). The magnetic history of this sample, coupled with its slow (millions of years) cooling time scale, suggests that the Moon had a core dynamo at 4.2 billion years ago (Ga). This re-

sult is consistent with recent analyses of Apollo-era seismic data (5) and lunar laser ranging (6) that indicate that even today the Moon has a small (~330 km in diameter) partially molten metallic core.

The lifetime of the early lunar dynamo remains uncertain. Thermochemical core convection owing to secular planetary cooling, which is widely thought to power most, if not all, dynamos in the present-day solar system (7), is not expected to have persisted beyond ~4.2 Ga (8, 9). Therefore, evidence that the dynamo continued after this time would probably indicate that it was powered by an alternative energy source (10, 11). Here we report a paleomagnetic study of another lunar sample with high magnetic recording fidelity, mare basalt 10020. This sample has the potential to contain a record of lunar magnetism 500 million years (My) after troctolite 76535 and has a much simpler thermal history. Furthermore, 10020 formed during a putative high-field epoch of the Moon, when paleofields may have exceeded even that of Earth today (1).

10020 was collected on 20 July 1969 as unoriented regolith float from the southwestern edge of Mare Tranquillitatis. Along with the

other Apollo 11 basalt samples, 10020 is thought to have been excavated from mostly intact bedrock by the impact that created West Crater at ~102 million years ago (Ma) [see supporting online material section 5 (SOM 5) and (12)]. 10020 is a fine-grained, vesicular, low-potassium ilmenite basalt of petrologic group B3 (13), with primary igneous glass (14, 15) and no apparent shock features [SOM 5 and (16)]. Its primary ferromagnetic mineral is kamacite (α-$Fe_{1-x}Ni_x$ with $x < 0.02$) [SOM 5 and (16)]. Our petrologic observations (SOM 5) found that plagioclase shows no fracturing, mechanical twinning, or alteration to maskelynite, and olivine shows no undulatory extinction, indicating peak shock pressures <5 GPa. 10020 has an $^{40}Ar/^{39}Ar$ age of 3.72 ± 0.04 Ga (17, 18) [recalculated using modern decay constants (19)], which is within error of Rb/Sr crystallization ages of other group B3 Apollo 11 basalts (17, 18). A previous paleomagnetic investigation observed that two unoriented chips of 10020 displayed some of the most stable NRM of any studied lunar sample (blocked up to at least 50 to 65 mT) [(20) and fig. 30 in (1)], possibly a reflection of its relatively high glass content (SOM 5). The late-stage (≲1100°C) primary igneous cooling rate of 10020

[1]Department of Earth, Atmospheric, and Planetary Sciences, Massachusetts Institute of Technology (MIT), 77 Massachusetts Avenue, Cambridge, MA 02139, USA. [2]Department of Earth and Planetary Science, University of California, Berkeley, CA 94720, USA. [3]Berkeley Geochronology Center, 2455 Ridge Road, Berkeley, CA 94709, USA. [4]Centre Européen de Recherche et d'Enseignement, CNRS/Université Aix-Marseille 3, France. [5]University of Hawaii at Manoa, Honolulu, HI, USA.

*To whom correspondence should be addressed. E-mail: nuptse@mit.edu

Fig. 1. NRM in mare basalt 10020. Shown is a two-dimensional projection of the NRM vectors of subsamples 234b1, 234b2, and 234b4 during AF demagnetization. Solid symbols represent the end points of magnetization projected onto the horizontal N-E planes, and open symbols represent those projected onto the vertical Z-E planes. Peak fields for selected AF steps are labeled in microteslas. Arrows denote HC component directions determined from principal components analyses (PCA). The mass of each subsample is listed below the sample name. (**A**) Subsample 234b1. (**B**) Subsample 234b2. (**C**) Subsample 234b4.
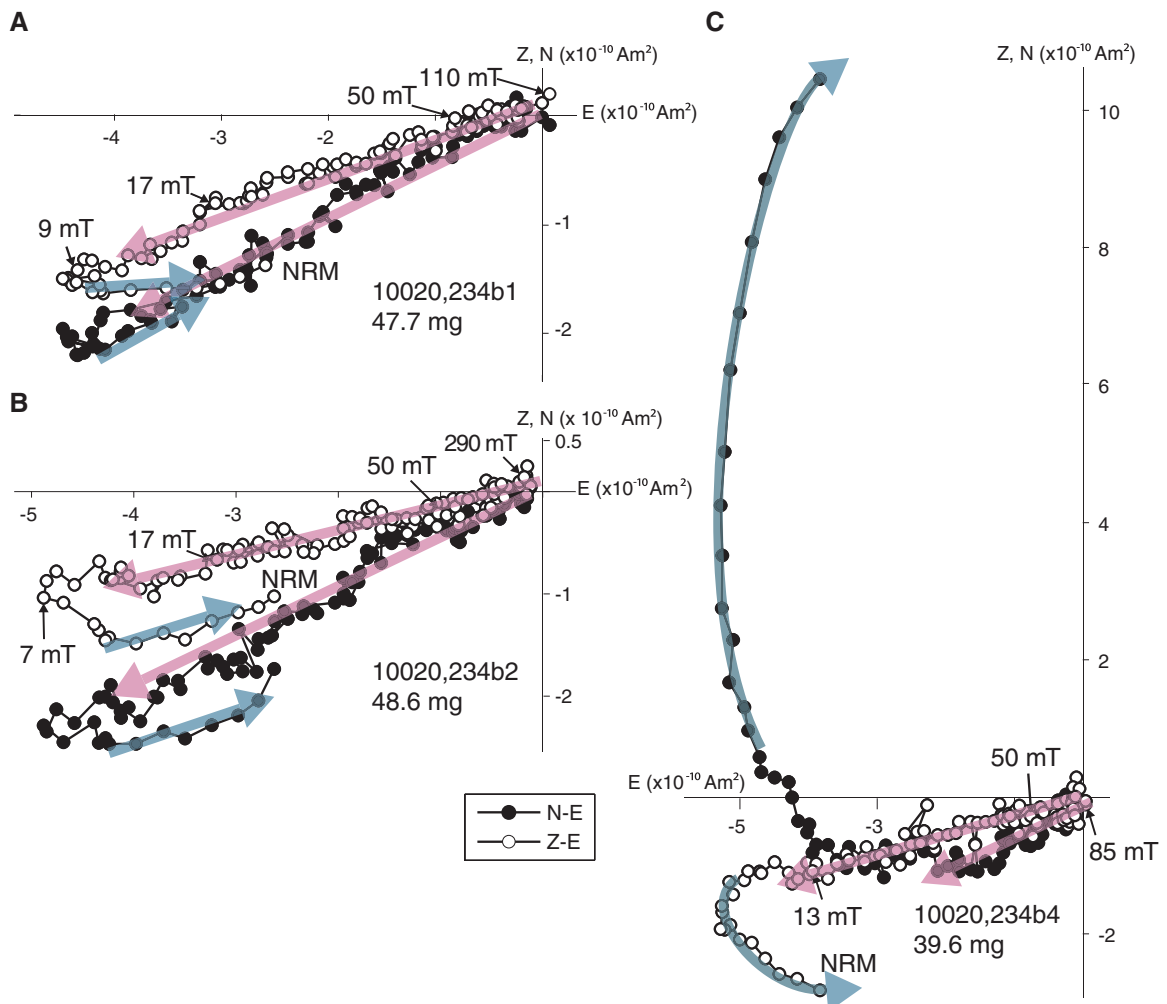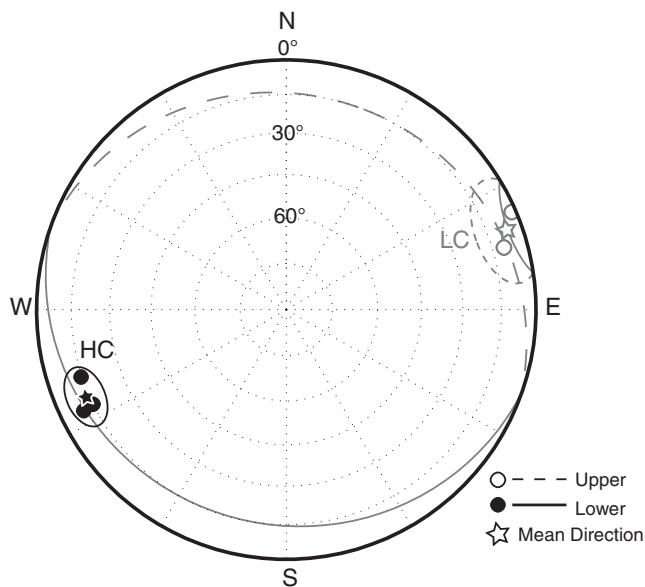
is estimated to have been 3°C hour^{-1} (13), using the maximum plagioclase width cooling indicator [SOM 5 and (21)]. Given that cooling rates are often slower at lower temperatures, this indicates that cooling and the acquisition of magnetization from the 780°C Curie temperature of kamacite to ambient lunar temperatures occurred over at least ~300 hours, far longer than the lifetime of modeled impact-generated fields.

These features make 10020 an ideal sample for testing the lunar dynamo hypothesis at 3.7 Ga. However, previous paleomagnetic analyses of 10020 (1, 20) did not demonstrate conclusively that the NRM originated on the Moon as a primary thermoremanence (TRM) (SOM 2). More importantly, these studies did not establish whether this field originated from a lunar dynamo or from transient impact-generated fields (SOM 2). We used nondestructive three-axis alternating field (AF) demagnetization to characterize the NRM component in two discrete sets of mutually oriented subsamples, one of which is discussed here and the other in SOM 2.

We identified a low-coercivity (LC) and high-coercivity (HC) component in each subsample (Figs. 1 and 2 and figs. S1 and S3). The LC component, blocked below ~17 mT, is approximately unidirectional at the scale of several millimeters but nonunidirectional at larger scales and has a relatively high ratio of NRM to isothermal remanent magnetization (IRM) (ranging up to 8%). These features suggest that the LC component is a secondary IRM resembling that observed in
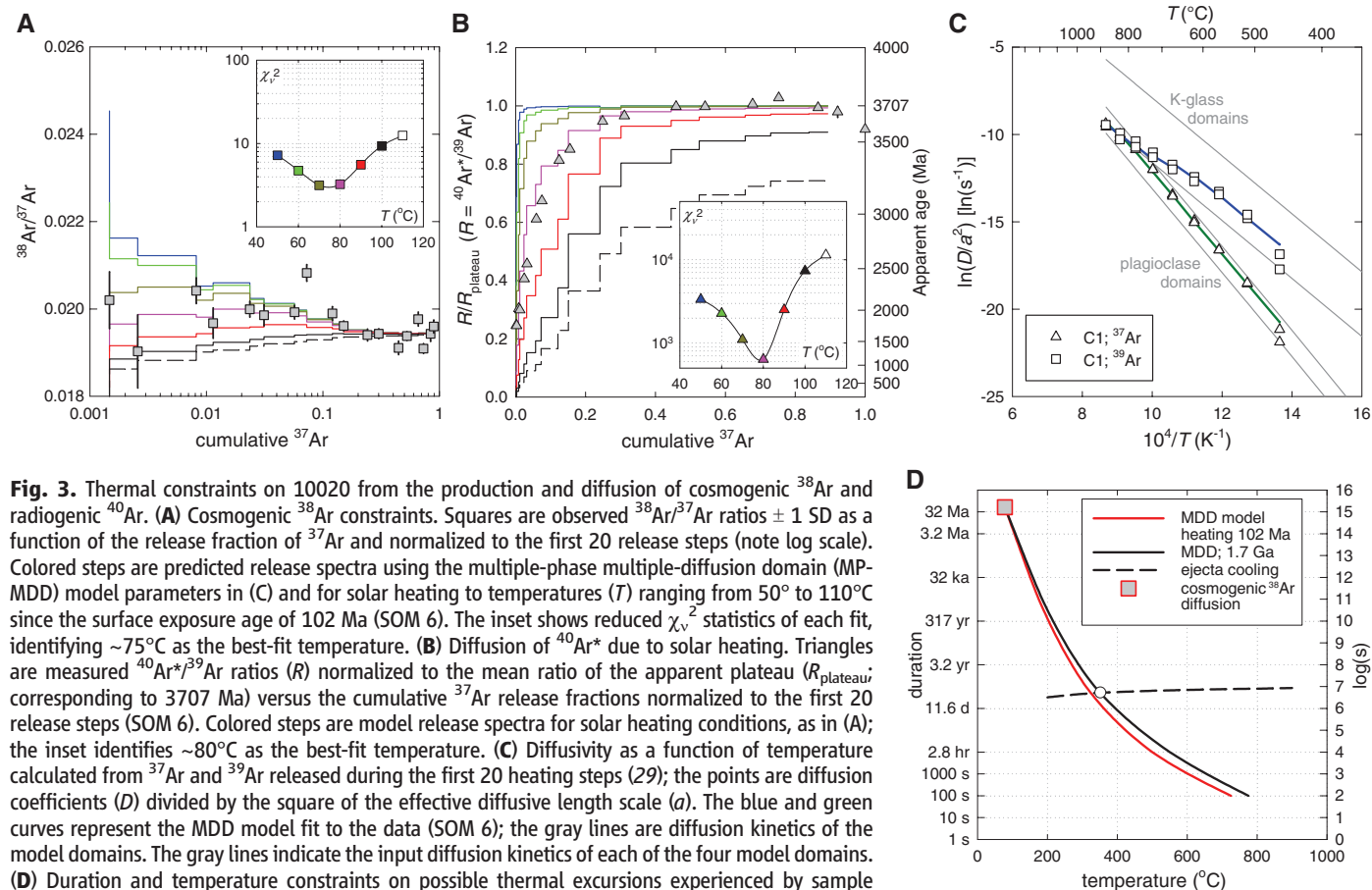

Fig. 2. Equal area stereographic projection of NRM component fits to 10020 subsamples 234b1, 234b2, and 232b4. Black circles denote HC directions for each subsample and light gray circles denote LC directions for samples 234b1 and 234b2. The LC component for sample 234b4 is less well constrained and lies somewhere on the gray great circle. Stars give mean directions for HC and LC components for the three subsamples, with surrounding ellipses indicating 95% formal confidence intervals on mean directions from PCA (not accounting for an additional ~3° to 5° of mutual orientation uncertainty). Solid and open symbols indicate the lower and upper hemisphere, respectively.

Fig. 3. Thermal constraints on 10020 from the production and diffusion of cosmogenic ^{38}Ar and radiogenic ^{40}Ar. (**A**) Cosmogenic ^{38}Ar constraints. Squares are observed ^{38}Ar/^{37}Ar ratios ± 1 SD as a function of the release fraction of ^{37}Ar and normalized to the first 20 release steps (note log scale). Colored steps are predicted release spectra using the multiple-phase multiple-diffusion domain (MP-MDD) model parameters in (C) and for solar heating to temperatures (T) ranging from 50° to 110°C since the surface exposure age of 102 Ma (SOM 6). The inset shows reduced χ_v^2 statistics of each fit, identifying ~75°C as the best-fit temperature. (**B**) Diffusion of ^{40}Ar* due to solar heating. Triangles are measured ^{40}Ar*/^{39}Ar ratios (R) normalized to the mean ratio of the apparent plateau ($R_{plateau}$; corresponding to 3707 Ma) versus the cumulative ^{37}Ar release fractions normalized to the first 20 release steps (SOM 6). Colored steps are model release spectra for solar heating conditions, as in (A); the inset identifies ~80°C as the best-fit temperature. (**C**) Diffusivity as a function of temperature calculated from ^{37}Ar and ^{39}Ar released during the first 20 heating steps (29); the points are diffusion coefficients (D) divided by the square of the effective diffusive length scale (a). The blue and green curves represent the MDD model fit to the data (SOM 6); the gray lines are diffusion kinetics of the model domains. The gray lines indicate the input diffusion kinetics of each of the four model domains. (**D**) Duration and temperature constraints on possible thermal excursions experienced by sample 10020. Solid curves are conditions at 1.7 Ga (black) and 102 Ma (red) that would best predict the observed ^{40}Ar*/^{39}Ar spectrum shown in (B) using the MP-MDD model in (C); the square is the best-fit solution from (A). The dashed curve predicts the time required to diffusively cool from an initial temperature T to <100°C in a 6-m-thick ejecta blanket (SOM 6). The intersection of this curve with the solid curve (open circle) gives the peak temperature that would explain the Ar data under this scenario.
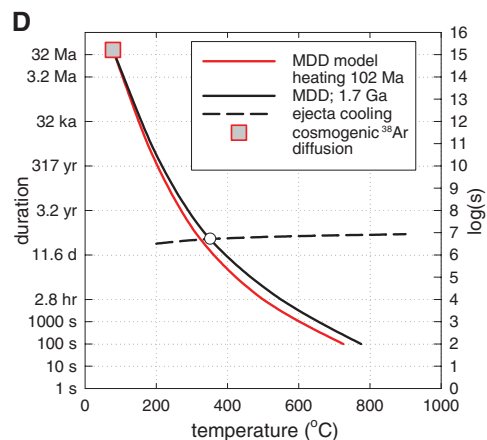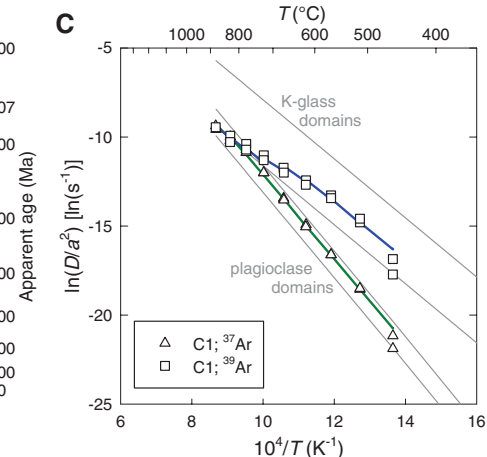
many other Apollo samples (*4, 22, 23*) and which is inferred to originate from handling after sampling on the Moon.

Depending on the subsample, the HC component is blocked from 8.5 to 17.5 mT up to >66 to 290 mT and decays linearly to the origin, suggesting that it is the final, primary component. Although the LC and HC components in the three 234b subsamples are antipodal (Fig. 2), other subsamples (SOM 2) do not show this relationship, making it unlikely that this has a rock magnetic source in general. The rate of decay of the HC component during AF demagnetization differs from that of a strong-field IRM or a weak-field pressure remanent magnetization (PRM) acquired at 1.8 GPa (the upper limit of our experimental setup), but is very similar to that of an anhysteretic remanent magnetization (ARM), an analog for TRM (SOM 3 and 4). Furthermore, our PRM acquisition experiments indicate that a very strong field (~700 µT) would have been necessary to produce the HC component if it were a shock remanent magnetization (SRM) (SOM 4). Our viscous remanent magnetization (VRM) acquisition experiments suggest that no more than 0.1% of the NRM could be a VRM acquired since the sample's arrival on Earth (SOM 4). These data collectively indicate that the HC component is very likely a TRM acquired during primary cooling in a field on the Moon.

The inferred paleointensities (SOM 3) for the HC components for our five subsamples, using anisotropy-corrected IRM and ARM methods, are 66 ± 37 µT and 55 ± 19 µT (uncertainty ranges are observed from multiple samples with 1 SD) with an overall mean value of 60 µT and estimated minimum value of ~12 µT (for comparison, Earth's surface field intensity is ~50 µT) (SOM 4). Such paleointensities are several orders of magnitude larger than that expected from external sources such as Earth, the Sun, the protoplanetary disk, or the Galaxy at 3.7 Ga (*4, 24*) and are nearly two orders of magnitude stronger than the strongest crustal remanent fields measured at the Apollo landing sites (*1*). The very slow cooling rate and lack of shock effects in 10020 suggest that the recorded field was temporally stable, like that expected from a core dynamo.

Although the crystallization age of 10020 is 3.7 Ga, its magnetization could have been acquired during subsequent thermal events. The lack of shock features precludes any brief, high-temperature shock-heating events associated with impacts, but temperature excursions such as those associated with low-grade metamorphism or burial in a hot ejecta blanket are possible. To assess this possibility, we conducted $^{40}Ar/^{39}Ar$ and $^{38}Ar/^{37}Ar$ thermochronometry on two whole-rock subsamples (SOM 6). We found that 10020 has a weighted average $^{40}Ar/^{39}Ar$ plateau age of 3705.6 ± 13.5 Ma [uncertainty 1 SD; includes uncertainty in the decay constant and the age of the fluence monitor (*25*)], which is indistinguishable from a previous study of this rock as well as

the mean crystallization age of other Apollo 11 group B3 basalts (*19*). The apparent spatial distributions of radiogenic ^{40}Ar ($^{40}Ar*$) and cosmogenic ^{38}Ar ($^{38}Ar_{cos}$) within plagioclase and glass (Fig. 3, A and B, and SOM 6) are consistent with diffusive loss of Ar due to heating to a constant temperature of ~80°C since the rock was exposed near the lunar surface at ~102 Ma [as indicated by cosmic ray exposure ages from (*17, 18*) and our measurements (SOM 6)]. This temperature is essentially the effective temperature equivalent to the expected Ar degassing solely due to solar heating integrated over the exposure age of 10020 (*26*). As has been concluded for many other Apollo 11 basalts (*26*), the only apparent thermal disturbance to 10020 since its formation at 3.70 Ga was from solar heating over the past 100 My (*27*).

Our data thus indicate that a dynamo field, and therefore an advecting metallic core, persisted on the Moon until at least as recently as ~3.70 Ga. It is not yet clear when the dynamo ceased activity. Combined with the paleomagnetic study of the 4.2-billion-year-old troctolite 76535 (*4*), our data imply a minimum lifetime of 500 My for the lunar dynamo, although it need not have been continuously active throughout the period spanned by these two samples. The lunar dynamo persisted until at least ~130 My after the estimated end of the late heavy bombardment [3.90 to 3.85 Ga (*28*)] and long after monotonic secular cooling models (*9*) predict that a core dynamo should have been active. Even nonmonotonic models involving the removal of thermal blankets from the core/mantle boundary do not unambiguously generate a dynamo after ~4.4 Ga (*8*). Potential alternative mechanisms for generating a late lunar dynamo are mechanical stirring of the core by precession (*11*) or by the impact of large bolides (*10*). These models predict surface fields at 3.7 Ga of ~0.2 to 15 µT, although this range is uncertain given that it is derived from scaling laws estimated for convection-driven dynamos. Nevertheless, these values are well below our mean 60 µT paleointensity estimate and barely overlap our minimum 12 µT estimate from 10020. Therefore, the late, intense paleomagnetic record from 10020 presents a challenge to current dynamo theory.

References and Notes

1. M. Fuller, S. M. Cisowski, in *Geomagnetism,* J. A. Jacobs, Ed. (Academic Press, Orlando, FL, 1987), vol. 2, pp. 307–455.
2. L. L. Hood, N. A. Artemieva, *Icarus* **193**, 485 (2008).
3. D. A. Crawford, P. H. Schultz, *Int. J. Impact Eng.* **23**, 169 (1999).
4. I. Garrick-Bethell, B. P. Weiss, D. L. Shuster, J. Buz, *Science* **323**, 356 (2009).
5. R. C. Weber, P.-Y. Lin, E. J. Garnero, Q. Williams, P. Lognonné, *Science* **331**, 309 (2011).
6. J. R. Williams, D. H. Boggs, C. F. Yoder, J. T. Ratcliff, J. O. Dickey, *J. Geophys. Res.* **106**, 27933 (2001).
7. D. J. Stevenson, *Space Sci. Rev.* **152**, 651 (2010).
8. D. R. Stegman, A. M. Jellinek, S. A. Zatman, J. R. Baumgardner, M. A. Richards, *Nature* **421**, 143 (2003).
9. W. Konrad, T. Spohn, *Adv. Space Res.* **19**, 1511 (1997).
10. M. Le Bars, M. A. Wieczorek, Ö. Karatekin, D. Cébron, M. Laneuville, *Nature* **479**, 215 (2011).
11. C. A. Dwyer, D. J. Stevenson, F. Nimmo, *Nature* **479**, 212 (2011).
12. D. W. Beaty, A. L. Albee, *Proc. Lunar Planet. Sci. Conf. 11th,* 23 (1980).
13. D. W. Beaty, A. L. Albee, *Proc. Lunar Planet Sci. Conf. 9th,* 359 (1978).
14. E. Roedder, P. W. Weiblen, *Proc. Apollo 11 Lunar Sci. Conf.,* 801 (1970).
15. M. R. Dence, J. A. V. Douglas, A. G. Plant, R. J. Traill, *Proc. Apollo 11 Lunar Sci. Conf.,* 315 (1970).
16. S. E. Haggerty, F. R. Boyd, P. M. Bell, L. W. Finger, W. B. Bryan, *Proc. Apollo 11 Lunar Sci. Conf.,* 513 (1970).
17. J. Geiss et al., *Philos. Trans. R. Soc. London Ser. A* **285**, 151 (1977).
18. S. Guggisberg et al., *Proc. Lunar Planet. Sci. Conf. 10th,* 1 (1979).
19. G. A. Snyder, D.-C. Lee, L. A. Taylor, A. N. Halliday, E. A. Jerde, *Geochim. Cosmochim. Acta* **58**, 4795 (1994).
20. D. W. Collinson, S. K. Runcorn, A. Stephenson, A. J. Manson, *Proc. Lunar Sci. Conf. 3rd,* 2343 (1972).
21. T. L. Grove, D. Walker, *Proc. Lunar Sci. Conf. 8th,* 1501 (1977).
22. K. P. Lawrence, C. L. Johnson, L. Tauxe, J. Gee, *Phys. Earth Planet. Inter.* **168**, 71 (2008).
23. G. W. Pearce, D. W. Strangway, *Apollo 16 Preliminary Science Report. NASA SP-315* (NASA, Washington, DC, 1972), pp. 7–55 to 7–58.
24. B. P. Weiss et al., *Science* **322**, 713 (2008).
25. P. R. Renne, G. Balco, K. Ludwig, R. Mundil, K. Min, *Geochim. Cosmochim. Acta* **75**, 5097 (2011).
26. G. Turner, *Earth Planet. Sci. Lett.* **11**, 169 (1971).
27. Some other thermal histories cannot be excluded by the Ar data alone. However, the combination of Ar data with geologic constraints strongly favors solar heating as the only major thermal disturbance after primary cooling (SOM 6).
28. C. R. Chapman, B. A. Cohen, D. H. Grinspoon, *Icarus* **189**, 233 (2007).
29. H. Fechtig, S. T. Kalbitzer, in *Potassium Argon Dating,* O. A. Schaeffer, J. Zahringer, Eds. (Springer-Verlag, New York, 1966), pp. 68–107.

Supporting Online Material